The Astrophysical Journal Supplement Series, 271:27 (12pp), 2024 March https://doi.org/10.3847/1538-4365/ad20c8

Jet Mechanism and γ-Ray-emitting Region for Fermi Flat-spectrum Radio Quasars with Broad-line Emissions

Lixia Zhang[1,2,3,4], Xiaobiao Chen[1], Shihui He[1], Wenwen Nie[1], Wentao Tang[1], Jiawei Huang[1], Guohai Chen[1], and Junhui Fan[1,2,3,4]
[1] Center for Astrophysics, Guangzhou University, Guangzhou 510006, People's Republic of China; lxzhang@gzhu.edu.cn, fjh@gzhu.edu.cn
[2] Astronomy Science and Technology Research Laboratory of Department of Education of Guangdong Province, Guangzhou 510006, People's Republic of China
[3] Key Laboratory for Astronomical Observation and Technology of Guangzhou, Guangzhou 510006, People's Republic of China
[4] Great Bay Center, National Astronomical Data Center, Guangzhou 510006, People's Republic of China
Received 2023 October 17; revised 2024 January 16; accepted 2024 January 19; published 2024 March 1

Abstract

Blazars are a subject of intense debate, specifically regarding their jet launch and emission mechanisms, and the origins of their γ-ray radiation. To explore these issues, we have built a comprehensive sample of flat-spectrum radio quasars (FSRQs), with well-characterized spectral energy distribution. This study aims to elucidate the dominant jet launch mechanism and the main processes behind the inverse Compton (IC) component. Additionally, we seek to pinpoint the location of the γ-ray dissipation region relative to the central black hole, denoted as R_γ. Our approach involves a detailed analysis of broad-line region (BLR) emission, from which we derive robust estimates of the black hole masses using two distinct virial techniques. This enables us to constrain the jet power across a wide array of FSRQs. Our findings lead to several significant conclusions: (i) The correlation of jet power with black hole mass allows us to test the Blandford–Znajek, Blandford–Payne, and hybrid mechanisms. We find that the hybrid mechanism is most effective in explaining the jet power observed in the majority of FSRQs; (ii) The IC component of the γ-rays in FSRQs is predominantly due to the external Compton process. (iii) Through simulations, we determine the minimum and maximum values of R_γ (the γ-ray dissipation region) and conclude it is located outside the BLR. This conclusion is derived from the variability timescale analysis.

Unified Astronomy Thesaurus concepts: Active galactic nuclei (16); Blazars (164); Flat-spectrum radio quasars (2163); Jets (870); Black holes (162)

1. Introduction

Blazars represent the most powerful and extreme subset of active galactic nuclei (AGNs), characterized by their unique observational features. These distinctive properties mainly stem from relativistic jets that are closely aligned with our line of sight, typically within a narrow angle of around 10°. Such an alignment results in a pronounced relativistic beaming effect, which significantly amplifies their observed emissions (Blandford & Rees 1978; Angel & Stockman 1980; Abdo et al. 2010a, 2010b; Acero et al. 2015; Ackermann et al. 2015; Ajello et al. 2020; Zheng et al. 2020; Fan et al. 2021; Abdollahi et al. 2022; Fan et al. 2023). According to the rest-frame equivalent width (EW) of emission lines, blazars can be classified as flat-spectrum radio quasars (FSRQs) and BL Lacertae objects (BL Lacs). FSRQs present broad emission lines with characterized EW > 5 Å, whereas BL Lacs show featureless spectra or weak emissions with EW < 5 Å (Urry & Padovani 1995; Scarpa & Falomo 1997). Blazars are also classified based on the logarithmic peak frequency of their spectral energy distributions (SEDs) into several categories: low synchrotron peaked (LSP) blazars, intermediate synchrotron peaked (ISP) blazars, high synchrotron peaked (HSP) blazars, and extreme high synchrotron peaked blazars. For further details, please refer to the following sources: Costamante et al. (2001), Abdo et al. (2010c), Arsioli et al. (2015), Fan et al. (2016), Arsioli & Polenta (2018), MAGIC Collaboration et al. (2020), and Yang et al. (2022).

The launch of the jets is essential for the central engine within AGNs and powerful blazars, as a way to dissipate angular momentum and allow accretion into the central object (Blandford & Payne 1982). The jet launch is frequently described by the Blandford–Znajek (BZ) process (Blandford & Znajek 1977) or the Blandford–Payne (BP) process (Blandford & Payne 1982). The BZ process extracts the rotational energy from a spinning black hole, whereas the BP process releases the gravitational energy of an accretion disk. Since both the BZ and BP mechanisms are maintained by the accretion of surrounding material into a central black hole, it can be inferred that there is a correlation between accretion and jet power (Maraschi & Tavecchio 2003). Additionally, there is a third mechanism, the hybrid jet model, which describes the formation of jets, through a combination of the BZ and BP mechanisms (Meier 2001; Garofalo et al. 2010).

From the perspective of observational analysis, the broadband SED from radio to high-energy γ-ray is characterized by a double bump structure in the $\log \nu f_\nu$ versus $\log \nu$ plane (Gehrels 1997). According to the prevalent lepton model, the low-energy bump is the synchrotron component, attributed to the synchrotron emission created by relativistic electrons propagating along the jet's magnetic fields (Rybicki & Lightman 1979). The high-energy bump is referred to as the inverse Compton (IC) component, and it emerges from the IC emission, derived from the relativistic electrons in the jet, that upscatter low-energy photons (IR to UV) to the highest energies (Massaro et al. 2004, 2006). Despite these correlations, the origin of the soft photons, which are scattered by the IC process, is a topic of ongoing debate. In the case of IC scattering, the process is called synchrotron-self-Compton (SSC) when the seed photons are derived from synchrotron emission (Rees 1967; Jones et al. 1974; Marscher & Gear 1985; Maraschi et al. 1992; Sikora et al. 1994; Bloom & Marscher 1996). Otherwise, the process is named external Compton (EC) when the seed photons originate from outer regions (outside the jet), including sources such as accretion disk (Dermer & Schlickeiser 1993), the broad-line region (BLR; Sikora et al. 1994), or the dust torus (DT; Błażejowski et al. 2000). In powerful blazars, especially FSRQs, the EC process offers a compelling explanation for their high-energy emissions. This process is a specific manifestation of the IC phenomenon, where relativistic electrons in the jet upscatter external seed photons to higher energies. The sources of these EC photons are typically intense external photon fields, comprising a mixture of components such as seed photons emanating from the accretion disk, the BLR, and the DT.

There has been significant attention devoted to the research concerning the location of the γ-ray-emitting region, to better understand the origin of the ambient photon field inside the jet (Agudo et al. 2011; Dotson et al. 2012; Nalewajko et al. 2014; Böttcher & Els 2016). Two key diagnostic tools are instrumental in locating the energy dissipation region: (i) variability timescale (Abdo et al. 2010d; Liu et al. 2011; Ramakrishnan et al. 2015); (ii) SED fitting (Dermer et al. 2009; Kang et al. 2014; Zheng et al. 2017; Tan et al. 2020). Despite these efforts, a consensus on the exact location of the energy dissipation region has not yet been reached. Some researchers have found that the absorption processes can account for the position of a γ-ray break through photon–photon pair production, suggesting that the γ-ray-emitting region is located in close proximity to the black hole (Poutanen & Stern 2010). Conversely, other researchers have proposed that the γ-ray-emitting region is situated further away from the black hole, partly based on the analysis of the γ-ray data obtained from the Fermi Large Area Telescope (LAT; Madejski & Sikora 2016; Zheng & Yang 2016; Zheng et al. 2017; Arsioli & Chang 2018; Jiang et al. 2020; Tan et al. 2020; Barat et al. 2022).

In this study, the primary objectives are to determine two critical aspects of FSRQs, Which mechanism dominates the jet-launching process? Where is the γ-ray-emitting region located, inside or outside the BLR? We rely on black hole masses derived from the broad-line emissions collected from the literature (Zhang et al. 2020; Paliya et al. 2021; Zhang et al. 2022; Chen et al. 2024). Moreover, we determine the jet power based on a broadband fit accounting for the synchrotron and IC components. The structure of this study is as follows: Section 2 provides details of the sample and methods, Section 3 presents the results and a discussion, and Section 4 outlines our conclusions. The cosmological constant used is from the ΛCDM model with $H_0 = 71\,\mathrm{km\,s^{-1}\,Mpc^{-1}}$, $\Omega_\Lambda = 0.73$, and $\Omega_M = 0.27$ (Komatsu et al. 2011).

2. Sample and Methods

2.1. γ-Ray Emissions

In this study, synchrotron and IC SEDs from Yang et al. (2022) and Yang et al. (2023) were collected for a broad range of blazars. We selected FSRQs containing both synchrotron and IC SEDs for further evaluation. These were compared with the data released in the Fourth Fermi-LAT 14 yr source catalog (4FGL-DR4; Ballet et al. 2023), resulting in an overall sample of 751 FSRQs. The classification of these target FSRQs was matched with the 4FGL-DR4 catalog, and their BLR emissions were compiled from published literature. Ultimately, we identified 557 FSRQs featuring both broadband SEDs and BLR emissions; this includes one HSP FSRQ, 94 ISP FSRQs, and 462 LSP FSRQs. The complete data set is tabulated in Table 1.

The γ-ray luminosity, as informed by the data from the Fermi-LAT catalog, is computed using the following formula:

$$L_\gamma = 4\pi d_{\mathrm{L}}^2 (1+z)^{\alpha_{\mathrm{ph}}-2} F, \tag{1}$$

where $d_{\mathrm{L}} = (1+z)\cdot \frac{c}{H_0} \cdot \int_1^{1+z} \frac{1}{\sqrt{\Omega_{\mathrm{M}} x^3 + 1 - \Omega_{\mathrm{M}}}} dx$ represents the luminosity distance, α_{ph} denotes the photon spectral index, and F corresponds to the integral flux in units of GeV cm^{-2} s^{-1}. Notably, F is calculated using the equation below, provided α_{ph} equates to 2:

$$F = N_{(E_{\mathrm{L}}\sim E_{\mathrm{U}})} \left(\frac{1}{E_{\mathrm{L}}} - \frac{1}{E_{\mathrm{U}}}\right) \ln \frac{E_{\mathrm{U}}}{E_{\mathrm{L}}}. \tag{2}$$

However, for cases where α_{ph} does not equal 2, F is calculated as follows:

$$F = N_{(E_{\mathrm{L}}\sim E_{\mathrm{U}})} \frac{1-\alpha_{\mathrm{ph}}}{2-\alpha_{\mathrm{ph}}} \frac{(E_{\mathrm{U}}^{2-\alpha_{\mathrm{ph}}} - E_{\mathrm{L}}^{2-\alpha_{\mathrm{ph}}})}{(E_{\mathrm{U}}^{1-\alpha_{\mathrm{ph}}} - E_{\mathrm{L}}^{1-\alpha_{\mathrm{ph}}})}. \tag{3}$$

Within this context, $N_{(E_{\mathrm{L}}\sim E_{\mathrm{U}})}$ represents the number of photons between energy E_{L} and E_{U}, reflecting 1 and 100 GeV, respectively. Detailed information can be found in the following references: Abdo et al. (2010a) and Fan et al. (2013a, 2013b).

2.2. Emission from the BLR

The optical spectra from FSRQs usually exhibit one or more broad emission lines: namely Hα, Hβ, Mg II, and C IV. This study compiles BLR emissions from three sources. First, a data set cited from Paliya et al. (2021) and its related references (abbreviated as P21) was utilized. Second, a collection from Zhang et al. (2020, 2022) and their respective references (briefly denoted as Z22), was employed. Lastly, new extensions from our preliminary work cited from Chen et al. (2024) (marked as C24) were added. These expanded FSRQs collected from C24 had their full width at half maximum (FWHM) and continuum luminosities related to emission lines derived with the available software PyQSOFit (Guo et al. 2018). This software computes parameter uncertainties using the Monte Carlo technique. Furthermore, a sophisticated approach involving the decomposition of the original spectrum into the target spectrum and host galaxy emission was implemented, using the principal component analysis (PCA) method. The line-free continuum was subtracted from the target spectrum by considering a power law and a third-order polynomial, along with optical and UV Fe II templates. Thus, we solely emphasize the broad emission line component in the target spectrum. The broad emission lines are effectively mimicked when an emission peak is not less than 3 rms (Zhang et al. 2020), and they were fitted in the following wavelength ranges: 6400–6800 Å for Hα, 4640–5100 Å for Hβ, 2700–2900 Å for Mg II, and 1500–1700 Å for C IV. For these broad emission

Table 1
SEDs for the Sample

Name (1)	Class (2)	z (3)	$\log L_{\rm BLR}$ (4)	Line (5)	References (6)	$\log(M/M_{\odot})_{\rm BLR}$ (7)	Line (8)	$\log(M/M_{\odot})_{\rm con}$ (9)	References (10)	$\log L_{\gamma}$ (11)	$\log L_{\rm sy}^{\rm p}$ (12)	$\log L_{\rm IC}^{\rm p}$ (13)
J0001.5+2113	LSP	1.106	43.65	Hα, Hβ, Mg II	P21	7.36	Hα, Hβ, Mg II	7.54	P21	46.68	46.17	47.21
J0004.3+4614	LSP	1.810	45.07	C IV	P21	8.43	C IV	8.36	P21	46.77	45.93	46.84
J0004.4-4737	LSP	0.880	44.10	Mg II	P21	7.94	Mg II	8.28	P21	46.00	45.96	45.89
J0005.9+3824	LSP	0.234	42.80	Hα, Hβ	C24	7.57	Hβ	7.35	TW	44.40	44.87	44.98
J0010.6+2043	ISP	0.600	44.35	Hβ, Mg II	P21	7.89	Hβ, Mg II	7.86	P21	45.13	44.54	45.04
J0011.4+0057	LSP	1.491	44.71	C IV, Mg II	P21	8.56	C IV, Mg II	8.66	P21	46.89	46.3	46.50
J0013.0+3355	LSP	1.682	44.58	C IV, Mg II	C24	9.68	Mg II	9.36	TW	46.48	45.87	45.84
J0013.6-0424	LSP	1.075	44.03	Mg II	P21	7.71	Mg II	7.82	P21	45.98	45.54	45.53
J0016.2-0016	LSP	1.576	44.77	C IV, Mg II	P21	8.51	C IV, Mg II	8.52	P21	46.61	45.61	47.02
J0016.5+1702	LSP	1.720	44.74	C IV, Mg II	P21	8.91	C IV, Mg II	8.88	P21	46.22	45.92	46.88

Note. Column (1): name from 4FGL-DR4; column (2): classification from synchrotron peak frequency; column (3): redshift (z); column (4): logarithm of the BLR luminosity in units of ergs per second ($\log L_{\rm BLR}$); column (5): estimators for BLR luminosity, including lines of Hα, Hβ, C IV, and Mg II; column (6): references for BLR luminosity; column (7): logarithm of the black hole mass estimated with BLR emission in units of solar mass ($\log(M/M_{\odot})_{\rm BLR}$); column (8): estimators for black hole mass, including lines of Hα, Hβ, CIV, Mg ll; column (9): logarithm of the black hole mass estimated with continuum emission in units of solar mass ($\log(M/M_{\odot})_{\rm con}$); column (10): the references for black hole mass. The references in columns (6) and (10) correspond to the literature such as Zhang et al. (2020, 2022), Paliya et al. (2021), and Chen et al. (2024). The symbol "TW" signifies that we calculate the black hole mass in this study. Column (11): logarithm of the γ-ray luminosity in units of ergs per second ($\log L_{\gamma}$); column (12): logarithm of the synchrotron peak luminosity in units of ergs per second ($\log L_{\rm sy}^{\rm p}$); column (13): logarithm of the IC peak luminosity in units of ergs per second ($\log L_{\rm IC}^{\rm p}$);

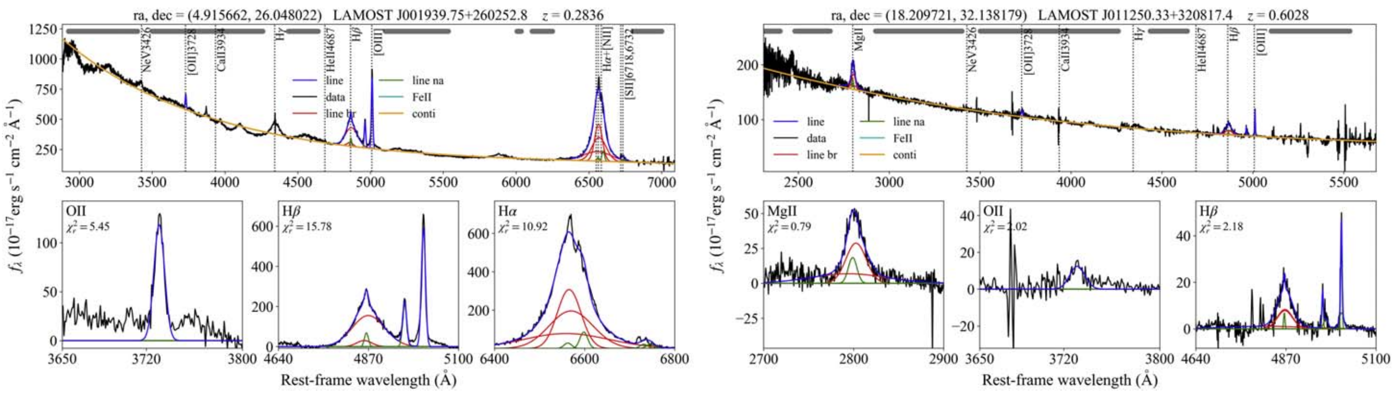

Figure 1. The optical spectra from LAMOST of 4FGL J0018.8+2611 (left) and 4FGL J0112.8+3208 (right), which are modeled with PyQSOFit. The black line shows the original spectral data, the orange line models the continuum, and the cyan line plots the optical and UV Fe II templates, as shown in the main graph. The red and green lines represent the broad and narrow components of the emission line, and the blue line is the sum of all the emission components, the Gaussian fitting of the emission lines of O II, Hβ, and Hα are shown in the corresponding three subgraphs.

lines, their narrow and broad components are fitted with single and multiple Gaussian functions, respectively. This resulted in the luminosity of each broad emission line being calculated by integrating the corresponding flux using the formula: $L_\lambda = 4\pi d_L^2 \lambda F(\lambda)$, and $\lambda F(\lambda)$ is the flux density integrated over the Gaussian functions of the broad emission lines, given in terms of GeV cm^{-2} s^{-1}. Two exemplar objects expanded using this adopted method are shown in Figure 1.

Based on the line luminosity outlined in Francis et al. (1991) and Celotti et al. (1997) (for Hα line), a ratio value of 100 is designated to $L_{y\alpha}$, and the total BLR fraction then becomes $\langle L_{\rm BLR}\rangle = 5.56 L_{y\alpha}$. With this, the BLR luminosity can be calculated using the following equation:

$$L_{\rm BLR} = L_{\rm line}\frac{\langle L_{\rm BLR}\rangle}{L_{\rm line,frac}}, \tag{4}$$

where $L_{\rm line}$ denotes the emission-line luminosity, while $L_{\rm line,frac}$ stands for the luminosity ratio. The luminosity ratios utilized are 77, 22, 34, and 63 for Hα, Hβ, Mg II, and C IV. In cases where two or more emission lines are presented for a single object in our sample, the geometric average is employed to obtain the total BLR luminosity.

2.3. Black Hole Mass

Reverberation mapping (RM) is a potent tool utilized to investigate the size, geometry, and kinematics of the BLR (Bahcall et al. 1972; Blandford & McKee 1982; Peterson 1993), as well as to establish determinations of black hole mass. The RM technique utilizes broad emission lines originating from photoionization produced by the continuum. The time it takes for light to travel from the ionization source to the BLR—the so-called time lag of light curve (τ), offers a means of calculating the BLR radius by the formula $R_{\rm BLR} = c\tau$, where c represents the speed of light. The implementation of the RM method upon virialized black hole mass has been achieved for 17 Seyfert 1 galaxies (Wandel et al. 1999) and 17 nearby quasars (Kaspi et al. 2000). Kaspi et al. (2000) derived an empirical relationship between BLR size and the monochromatic luminosity at 5100 Å considering 34 nearby AGNs. This empirical relation has found broad application as a black hole mass estimator in samples consisting of radio-quiet and purely radio-loud objects (Laor 2000; Gu et al. 2001). The relation presumes the BLR to be virialized. In this context, the continuum luminosity (λL_λ) represents the BLR radius, while the FWHM stands for the BLR velocity. Consequently, the virial black hole mass can be calculated from single-epoch optical spectra (Shen et al. 2011) as indicated in Equation (5):

$$\log\left(\frac{M_{\rm BH}}{M_\odot}\right) = a_* + b_*\log\left(\frac{\lambda L_\lambda}{10^{44}\ {\rm erg\ s^{-1}}}\right) + 2\log\left(\frac{\rm FWHM_{line}}{\rm km\ s^{-1}}\right). \tag{5}$$

The calibration coefficients in this equation, a_* and b_*, have the following values: $(a_*, b_*) = (0.672, 0.61)$ for Hβ (McLure & Dunlop 2004), $(a_*, b_*) = (0.505, 0.62)$ for Mg II (McLure & Dunlop 2004), and $(a_*, b_*) = (0.660, 0.53)$ for C IV (Vestergaard & Peterson 2006). See details from Zhang et al. (2022). It is also feasible to calculate the virial black hole mass from FWHM and BLR luminosity, and BLR luminosity serves as a substitute for continuum luminosity. This is exemplified in the Hα line with the resultant virial black hole mass recorded as expressed in Equation (6) (Shen et al. 2011):

$$\log\left(\frac{M_{\rm BH}}{M_\odot}\right)_{\rm H\alpha} = 0.379 + 0.43\log\left(\frac{L_{\rm H\alpha}}{10^{42}\ {\rm erg\ s^{-1}}}\right) + 2.1\log\left(\frac{\rm FWHM_{H\alpha}}{\rm km\ s^{-1}}\right). \tag{6}$$

Subsidiarily, when the continuum is supplanted with another broad line in Equation (5), the calibration coefficients can be derived as $(a_*, b_*) = (1.63 \pm 0.04, 0.49 \pm 0.03)$ for Hβ (Shaw et al. 2012), $(a_*, b_*) = (1.70 \pm 0.07, 0.63 \pm 0.00)$ for Mg II (Shen et al. 2011), and $(a_*, b_*) = (1.52 \pm 0.22, 0.46 \pm 0.01)$ for C IV (Shen et al. 2011). Both the virial black hole mass derived from the continuum ($\log(M/M_\odot)_{\rm con}$) and from the broad emissions ($\log(M/M_\odot)_{\rm BLR}$) are utilized in this work to examine the jet mechanism.

2.4. Jet Physical Parameters

Ghisellini (1996) established correlations between synchrotron luminosity and IC luminosity that allow one to ascertain whether the IC component is governed by the SSC process ($L(\nu^{\rm p}_{\rm SSC}) = L(\nu^{\rm p}_{\rm sy})^{1.0}$) or the EC process ($L(\nu^{\rm p}_{\rm EC}) = L(\nu^{\rm p}_{\rm sy})^{1.5}$). We then conducted an exploration of the correlation between

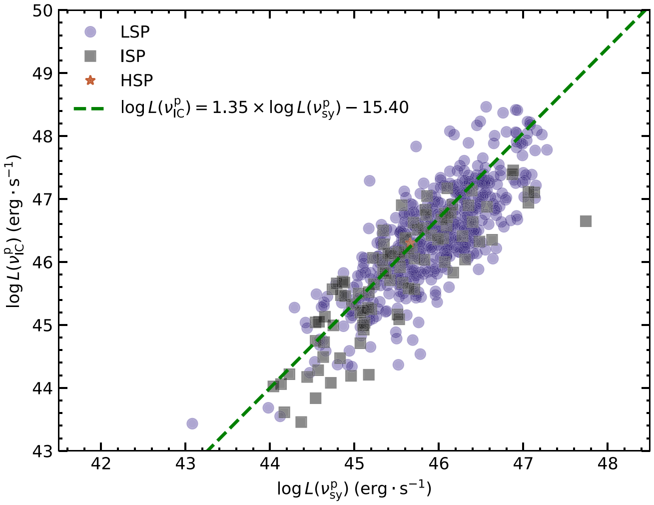

Figure 2. The IC peak luminosity as a function of the synchrotron peak luminosity, the solid blue circles are LSP FSRQs, the solid black squares are ISP FSRQs, and one solid red star is the HSP FSRQ. The green-dashed line is a linear fit to the $\log L(\nu^{\rm p}_{\rm IC})$ vs. $\log L(\nu^{\rm p}_{\rm sy})$ for the whole sample with the fit parameters.

IC peak and synchrotron peak luminosity, adopting a method of ordinary and symmetrical least-squares regression (OLS; see Feigelson & Babu 1992), as displayed in Figure 2. The linear fitting equation is provided as follows:

$$\log L(\nu^{\rm p}_{\rm IC}) = (-15.40 \pm 1.56) + (1.35 \pm 0.03)\log L(\nu^{\rm p}_{\rm sy}). \tag{7}$$

infer that the seed photons of FSRQs may originate from the external photon field, including BLR, DT, and accretion disks.

In the given scenario, the EC process dominates the IC component of FSRQ. The peak emission of the IC component may be transformed into the Klein–Nishina regime, under the condition that $\gamma_0 \Gamma h\nu_{\rm ext} \gtrsim m_{\rm e}c^2$. Here, γ_0 denotes the peak Lorentz factor of the electrons, h signifies the Planck constant, $\nu'_{\rm sy}$ represents the synchrotron peak frequency within the jet frames, $\nu_{\rm ext}$ refers to the external photon frequency in the AGN frame, and $m_{\rm e}$ is the electron mass. Based on our calculations, it is determined that the IC peaks of our sample primarily fall within the Thomson regimes, observing that $\gamma_0 \Gamma h\nu_{\rm ext} < m_{\rm e}c^2$.

Several authors reveal that the γ-ray emission region is located beyond the BLR but within the DT (Arsioli & Chang 2018; Tan et al. 2020; Barat et al. 2022). Accordingly, the γ-ray seed photons are inferred to originate from an infrared external photon field (Tramacere et al. 2010). For a thorough discussion, please refer to Section 3.3. Subsequently, the radiation from the infrared DT provides a typical value for the external photon frequency, denoted as $\nu_{\rm ext} = \nu_{\rm ext,DT} = 3 \times 10^{13}$ Hz (Ghisellini & Tavecchio 2009). We adopt an approximation of $\Delta t/(1+z) \approx 1$ day for Fermi blazars (Hu et al. 2014; Chen 2018). We also consider the curvature of the electron energy distribution as $b \sim 5|P_1|$ (Massaro et al. 2006; Chen 2014), where P_1 represents the synchrotron curvature as proposed by Yang et al. (2022). Consequently, using the input parameters from broadband SEDs, the jet physical parameters are derived based on a one-zone leptonic model in cgs units (e.g., Chen 2018 and Zhang et al. 2023):

$$\begin{cases}
\gamma_0 = 1641.5\left(\dfrac{\nu^{\rm p}_{\rm sy}}{10^{14}\,{\rm Hz}}\right)^{1/2}\left(\dfrac{\nu^p_{\rm ec}}{10^{22}\,{\rm Hz}}\dfrac{10^{14}\,{\rm Hz}}{\nu^p_{\rm sy}}\right)^{1/4}\left(\dfrac{\nu^p_{\rm sy}L(\nu^p_{\rm sy})}{10^{46}\,{\rm erg\,s^{-1}}}\right)^{-1/8}\left(\dfrac{\nu^p_{\rm SSC}L(\nu^p_{\rm SSC})}{\nu^p_{\rm sy}L(\nu^p_{\rm sy})}\right)^{1/8}\left(\dfrac{\nu_{\rm ext}}{3\times10^{13}\,{\rm Hz}}\right)^{-1/4}\left(\dfrac{\Delta t(1+z)}{1\,{\rm day}}\right)^{1/4}\left(\dfrac{b}{2}\right)^{1/16},\\
\delta = 9.63\left(\dfrac{\nu^p_{\rm ec}}{10^{22}\,{\rm Hz}}\dfrac{10^{14}\,{\rm Hz}}{\nu^p_{\rm sy}}\right)^{1/4}\left(\dfrac{\nu^p_{\rm sy}L(\nu^p_{\rm sy})}{10^{46}\,{\rm erg\,s^{-1}}}\right)^{1/8}\left(\dfrac{\nu^p_{\rm SSC}L(\nu^p_{\rm SSC})}{\nu^p_{\rm sy}L(\nu^p_{\rm sy})}\right)^{-1/8}\left(\dfrac{\nu_{\rm ext}}{3\times10^{13}\,{\rm Hz}}\right)^{-1/4}\left(\dfrac{\Delta t(1+z)}{1\,{\rm day}}\right)^{-1/4}\left(\dfrac{b}{2}\right)^{-1/16},\\
B = 1.03\left(\dfrac{\nu^p_{\rm ec}}{10^{22}\,{\rm Hz}}\dfrac{10^{14}\,{\rm Hz}}{\nu^p_{\rm sy}}\right)^{-3/4}\left(\dfrac{\nu^p_{\rm sy}L(\nu^p_{\rm sy})}{10^{46}\,{\rm erg\,s^{-1}}}\right)^{1/8}\left(\dfrac{\nu^p_{\rm SSC}L(\nu^p_{\rm SSC})}{\nu^p_{\rm sy}L(\nu^p_{\rm sy})}\right)^{-1/8}\left(\dfrac{\nu_{\rm ext}}{3\times10^{13}\,{\rm Hz}}\right)^{3/4}\left(\dfrac{\Delta t(1+z)}{1\,{\rm day}}\right)^{-1/4}\left(\dfrac{b}{2}\right)^{-1/16},\\
R = 2.49\times10^{16}\left(\dfrac{\nu^p_{\rm ec}}{10^{22}\,{\rm Hz}}\dfrac{10^{14}\,{\rm Hz}}{\nu^p_{\rm sy}}\right)^{1/4}\left(\dfrac{\nu^p_{\rm sy}L(\nu^p_{\rm sy})}{10^{46}\,{\rm erg\,s^{-1}}}\right)^{1/8}\left(\dfrac{\nu^p_{\rm SSC}L(\nu^p_{\rm SSC})}{\nu^p_{\rm sy}L(\nu^p_{\rm sy})}\right)^{-1/8}\left(\dfrac{\nu_{\rm ext}}{3\times10^{13}\,{\rm Hz}}\right)^{-1/4}\left(\dfrac{\Delta t(1+z)}{1\,{\rm day}}\right)^{3/4}\left(\dfrac{b}{2}\right)^{-1/16},\\
N_0 = 7.16\times10^{-3}\left(\dfrac{\nu^{\rm p}_{\rm sy}}{10^{14}\,{\rm Hz}}\right)^{-3/2}\left(\dfrac{\nu^p_{\rm ec}}{10^{22}\,{\rm Hz}}\dfrac{10^{14}\,{\rm Hz}}{\nu^p_{\rm sy}}\right)^{-1}\left(\dfrac{\nu^p_{\rm sy}L(\nu^p_{\rm sy})}{10^{46}\,{\rm erg\,s^{-1}}}\right)^{1/4}\left(\dfrac{\nu^p_{\rm SSC}L(\nu^p_{\rm SSC})}{\nu^p_{\rm sy}L(\nu^p_{\rm sy})}\right)^{3/4}\left(\dfrac{\nu_{\rm ext}}{3\times10^{13}\,{\rm Hz}}\right)\left(\dfrac{\Delta t(1+z)}{1\,{\rm day}}\right)^{-3/2}\left(\dfrac{b}{2}\right)^{3/8},\\
U_{\rm ext} = 3.23\times10^{-4}\left(\dfrac{\nu^p_{\rm ec}L(\nu^p_{\rm ec})}{\nu^p_{\rm sy}L(\nu^p_{\rm sy})}\right)\left(\dfrac{\nu^p_{\rm ec}}{10^{22}\,{\rm Hz}}\dfrac{10^{14}\,{\rm Hz}}{\nu^p_{\rm sy}}\right)^{-2}\left(\dfrac{\nu_{\rm ext}}{3\times10^{13}\,{\rm Hz}}\right)^{2}.
\end{cases} \tag{8}$$

A robust correlation exists between IC peak luminosity and synchrotron peak luminosity, as supported by Pearson ($r_{\rm p} = 0.86$, $p_{\rm p} = 2.44 \times 10^{-57}$), Spearman ($r_{\rm S} = 0.86$, $p_{\rm S} = 4.17 \times 10^{-58}$), and Kendall tau ($r_{\rm K} = 0.68$, $p_{\rm K} = 7.11 \times 10^{-44}$) correlation coefficients. This correlation has been reported by other authors as well (Abdo et al. 2010c; Gao et al. 2011; Zhang et al. 2012; Arsioli & Chang 2018; Chen et al. 2023). In this work, our regression analysis implies that the EC process likely dominates the IC component of FSRQs. This is suggested by the Equation (7) relationship $L(\nu^{\rm p}_{\rm EC}) \sim L(\nu^{\rm p}_{\rm sy})^{1.4}$, which closely aligns with the theoretical $L(\nu^{\rm p}_{\rm EC}) = L(\nu^{\rm p}_{\rm sy})^{1.5}$ correlation. We

In the above set of equations, γ_0 represents the peak Lorentz factor, δ stands for the Doppler factor, B signifies the magnetic field strength, R denotes the radius of the emission region, N_0 is the normalization for electron energy distribution, and $U_{\rm ext}$ is the external photon energy density. Based on these, we can determine the energy density of the Poynting flux ($U_{\rm B}$), electrons ($U_{\rm e}$), protons ($U_{\rm p}$), and radiation ($U_{\rm r}$). These parameters can then be used to calculate the jet power in four forms, as shown in Equation (9):

$$\begin{aligned} P_{\rm jet} &= 2\pi R^2 c\Gamma^2(U_{\rm B} + U_{\rm e} + U_{\rm p} + U_{\rm r}) \\ &= P_{\rm B} + P_{\rm e} + P_{\rm p} + P_{\rm r}, \end{aligned} \tag{9}$$

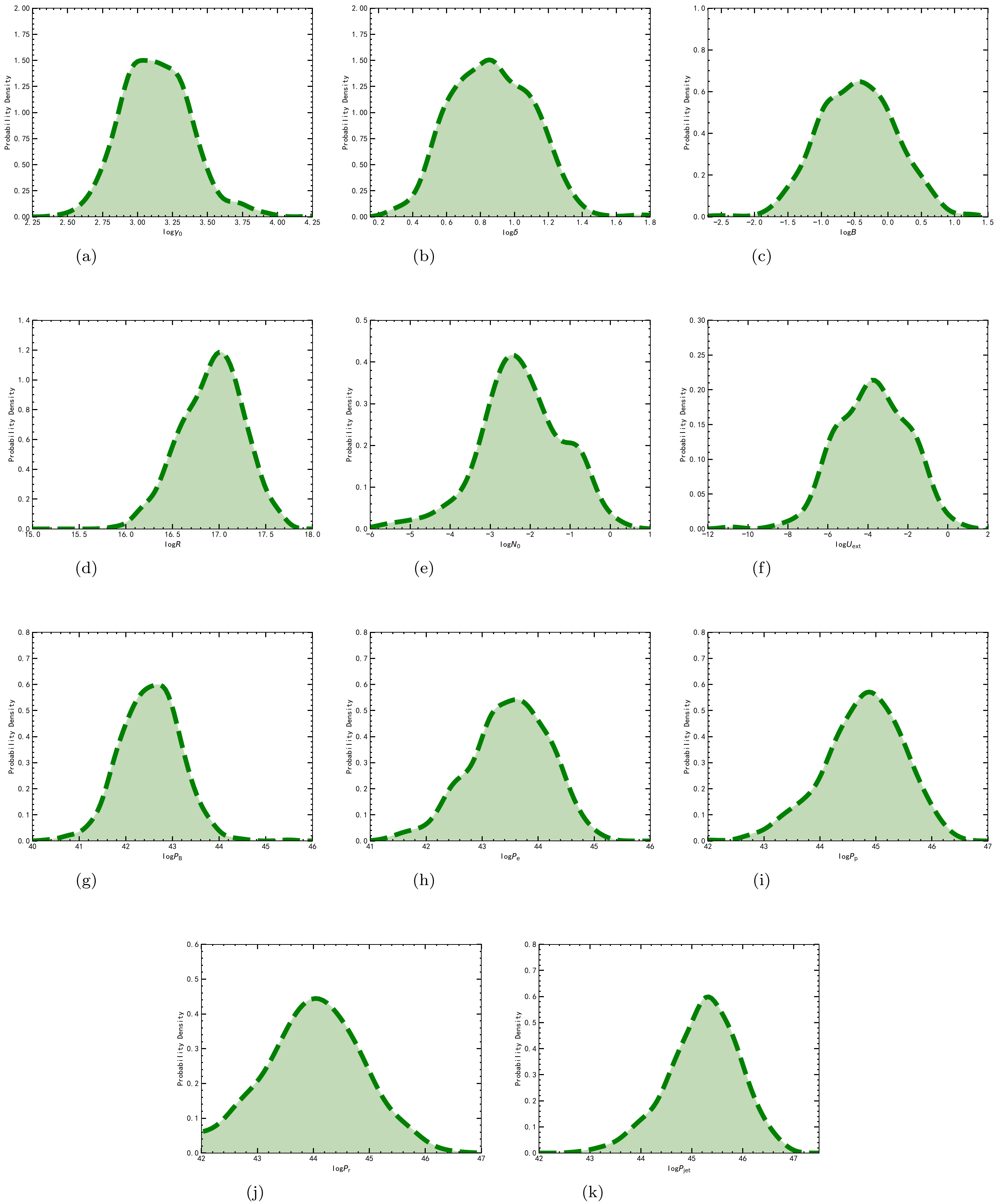

Figure 3. The distributions of physical parameters: (a) the peak Lorentz factor; (b) the Doppler factor; (c) the magnetic field strength in units of gauss; (d) the radius of the emission region in units of centimeters; (e) the normalization for electron energy distribution; (f) the external photon energy density; (g) the power in the form of Poynting flux in units of ergs per second; (h) the power in the form of electrons in units of ergs per second; (i) the power in the form of protons in units of ergs per second; (j) the power in the form of radiation in units of ergs per second; (k) the total jet power in units of ergs per second.

Table 2
Jet Physical Parameters

Name (1)	$\log \gamma_0$ (2)	$\log \delta$ (3)	$\log B$ (4)	$\log R$ (5)	$\log N_0$ (6)	$\log U_{\rm ext}$ (7)	$\log P_{\rm B}$ (8)	$\log P_{\rm e}$ (9)	$\log P_{\rm p}$ (10)	$\log P_{\rm r}$ (11)	$\log P_{\rm jet}$ (12)	$R_{\rm BLR}$ (13)	R_γ(min) (14)	R_γ(max) (15)
J0001.5+2113	2.92	0.59	0.20	16.65	−0.64	−1.28	42.76	43.40	44.58	44.90	45.38	0.022	3.66	6.87
J0004.3+4614	3.11	0.69	−0.38	17.00	−1.73	−2.78	42.49	43.65	44.81	44.79	45.42	0.111	3.46	6.49
J0004.4-4737	2.99	1.04	−0.59	17.00	−2.34	−4.88	42.78	43.50	44.71	43.32	45.05	0.036	4.20	7.86
J0005.9+3824	2.84	0.60	0.45	16.20	−0.91	−1.76	42.38	42.15	43.51	42.59	43.91	0.008	6.04	11.31
J0010.6+2043	3.43	0.69	−0.33	16.51	−2.74	−3.09	41.62	42.59	44.08	43.15	44.45	0.049	4.97	9.32
J0011.4+0057	3.25	0.90	−0.36	17.11	−2.97	−3.88	43.16	43.36	44.45	44.49	45.10	0.074	3.51	6.58
J0013.0+3355	3.37	1.33	−1.84	17.60	−4.01	−7.91	42.05	44.30	45.03	43.22	45.41	0.063	3.22	6.04
J0013.6-0424	3.47	1.32	−1.73	17.37	−4.14	−7.67	41.78	44.04	44.99	42.74	45.34	0.034	3.81	7.13
J0016.2-0016	3.00	0.67	−0.64	16.91	−0.87	−2.77	41.76	44.23	45.86	44.66	46.20	0.079	3.45	6.47
J0016.5+1702	2.92	0.63	−0.24	16.91	−0.96	−2.32	42.49	43.66	44.80	44.36	45.26	0.076	3.28	6.15

Note. Column (1): the name from 4FGL-DR4; column (2): logarithm of the peak Lorentz factor ($\log \gamma_0$); column (3): logarithm of the Doppler factor ($\log \delta$); column (4): logarithm of the magnetic field in units of gauss ($\log B$); column (5): logarithm of the emission region in units of centimeters ($\log R$); column (6): logarithm of the normalization for electron energy distribution ($\log N_0$); column (7): logarithm of the external photon energy density ($\log U_{\rm ext}$); column (8): logarithm of the jet power carried by magnetic field in units of ergs per second ($\log P_{\rm B}$); column (9): logarithm of the jet power carried by electrons in units of ergs per second ($\log P_{\rm e}$); column (10): logarithm of the jet power in protons in units of ergs per second ($\log P_{\rm p}$); column (11): logarithm of the jet power in radiation in units of ergs per second ($\log P_{\rm r}$); column (12): logarithm of the total jet power in units of ergs per second ($\log P_{\rm jet}$); column (13): the size of the BLR in units of parsecs ($R_{\rm BLR}$); column (14): the minimum size of the γ-rays in parsecs (R_γ(min)); column (15): the maximum size of the γ-rays in parsecs (R_γ(max)).

where "2" represents the existence of two jets, $U_{\rm B} = \frac{B^2}{8\pi}$, $U_{\rm e} = m_{\rm e}c^2\int N(\gamma)\gamma d\gamma$, $U_{\rm p} = m_{\rm p}c^2\int N(\gamma)d\gamma$ assuming one proton per electron, $U_{\rm r} = \frac{L^{\rm ob}/\delta^4}{4\pi R_{\rm b}^2 c}$ is assumed in the observational frame, and here we adopt $L^{\rm ob} = L_\gamma$ for our sample. Lastly, the terms $P_{\rm B}$, $P_{\rm e}$, $P_{\rm p,}$ and $P_{\rm r}$ represent the jet power of the magnetic field, relativistic electrons, cold protons, and radiation, respectively. The distributions for these jet physical parameters and jet power are depicted in Figure 3. The complete data set of jet physical parameters is tabulated in Table 2.

2.5. Magnetic Field of a Hot Corona

Since the corona can enhance the magnetic field, it is very important for the formation of jets. Detailed properties of the coronae above the disk require further clarification, despite extensive studies conducted by numerous scholars (Galeev et al. 1979; Haardt & Maraschi 1993; Svensson & Zdziarski 1994; Cao 2009). However, it can be affirmed that the hot corona is geometrically thick and optically thin (Cao 2018). Therefore, we consider that the strength of the magnetic field is advected by the hot corona for our sample in this study. Then the corona above the accretion disk can be described by the relative thickness $\tilde{H}_{\rm c} = H_{\rm c}/R$ and optical depth $\tau_{\rm c} = \rho_{\rm c} H_{\rm c} \kappa_{\rm T}$, where $H_{\rm c}$ and $\rho_{\rm c}$, respectively, represent the thickness and density of the corona, and $\kappa_{\rm T} = 0.4\ {\rm g}^{-1}\ {\rm cm}^2$ is the Compton scattering opacity. This creates the following equation for the gas pressure of the corona:

$$p_{\rm c} = \frac{\rho_{\rm c}}{2}\left(\frac{H_{\rm c}}{R}\right)^2 \frac{L_*^2}{R^2}. \tag{10}$$

As for the angular momentum, it is given by

$$L_*^2 = L^2 - j^2(E^2 - 1), \tag{11}$$

where L refers to the conserved angular momentum of the gas and E is the conserved energy, see details from Abramowicz et al. (1997). The gas angular momentum at the black hole horizon $L_*(r_{\rm h})$ is less than that at the marginally stable circular orbits $L_*(r_{\rm ms})$ (e.g., Abramowicz et al. 1996). In accordance with these restrictions, $L_* = L(r_{\rm ms})$ is utilized to compute the magnetic field strength for the maximum jet power in the work of Cao (2018). Moreover, a β parameter is used to describe the magnetic field strength of the corona: $p_{\rm m} = \frac{B_z^2}{8\pi} = \beta p_{\rm c}$. Here, B_z indicates the field strength in the corona, defined as

$$B_z = 4.37 \times 10^8 \beta^{1/2} \tau_{\rm c}^{1/2} \tilde{H}_{\rm c}^{1/2} m^{-1/2} r^{-3/2} L_*^2\ {\rm G}. \tag{12}$$

Complementary metrics include

$$m = \frac{M_{\rm BH}}{M_\odot},\ r = \frac{Rc^2}{GM_{\rm BH}}. \tag{13}$$

We know that the properties of coronae may be related to their hard X-ray emission. Assuming such a disk-coronal-jet model is indeed at work in our sample, then a correlation between radio and hard X-ray emission can be expected. Setting the X-ray energy spectral index as $\alpha_{\rm X} = 1$, consequently, the soft X-ray luminosity at 1 keV can be linearly converted into the hard X-ray luminosity at 2 keV, demonstrated as $L_{\rm X,1\ keV} = kL_{\rm X,2\ keV}$ (k is a constant). For the whole sample, a significant correlation is observed between 1 keV X-ray luminosity and 1.4 GHz radio luminosity, marked by the correlation coefficients and the significance level of Pearson ($r = 0.68$, $P = 9.53 \times 10^{-46}$), Spearman ($r = 0.72$, $P = 2.98 \times 10^{-53}$), and Kendall tau ($r = 0.55$, $P = 9.60 \times 10^{-49}$). Furthermore, the OLS regression gives a linear fitting equation as stated below:

$$\log L_{\rm X,1\ keV} = (-1.75 \pm 2.04) + (1.08 \pm 0.05)\log L_{\rm R,1.4\ GHz}. \tag{14}$$

Our findings, which combine the linear correlation of $L_{\rm X,1\ keV}$ versus $L_{\rm X,2\ keV}$ with Equation (14), also supports the model of disk-coronal-jet connection for our sample.

2.6. Jet Model

In the context of the BZ model, driven by a rapidly spinning black hole, the jet power can be calculated as described by

(MacDonald & Thorne 1982; Ghosh & Abramowicz 1997):

$$P_{\rm jet}^{\rm BZ} = \frac{1}{32}\omega_{\rm F}^2 B_{\rm h}^2 R_{\rm h}^2 c j^2. \tag{15}$$

The variables in this equation represent the following: $\omega_{\rm F}$ denotes the field lines angular velocity relative to the black hole angular velocity, $B_{\rm h}$ signifies the field strength at the black hole horizon $R_{\rm h}$, and j stands for the black hole spin. The maximum jet power within the BZ model framework can be derived by substituting Equation (12) into Equation (15):

$$P_{\rm jet}^{\rm BZ} = 39 \times 10^{36}\omega_{\rm F}^2 \beta\tau_{\rm c} m r_{\rm h}^{-1}\tilde{H}_{\rm c} L_*^2(r_{\rm h}) j^2 \text{ erg}. \tag{16}$$

In the BP model extracting the gravitational energy of an accretion disk, the jet power associated with it is calculated as (Livio et al. 1999)

$$P_{\rm jet}^{\rm BP} \sim \frac{B_z B_\phi^s}{2\pi} R_j \Omega \pi R_j^2, \tag{17}$$

where $B_\phi = \xi_\phi B_z$ refers to the azimuthal component of the field at the corona surface, R_j symbolizes the radius of the jet formation region within the corona, and Ω signifies the angular velocity of the gas in the corona. Upon integrating Equation (12) into Equation (17), we can obtain the BP jet power as

$$P_{\rm jet}^{\rm BP} \simeq 3.13 \times 10^{37} \xi_\phi \tilde{\Omega} r_j^{-1/2} m \beta \tau_{\rm c} \tilde{H}_{\rm c} \text{ erg s}^{-1}. \tag{18}$$

Given that a substantial part of gravity can be released in the inner region of the accretion disk, specifically, within a radius of about $2R_{\rm ms}$ (Shakura & Sunyaev 1973), then $R_j = 2R_{\rm ms}$ is considered for calculating the BP jet power (Cao 2018; Chen et al. 2022).

In the hybrid model, which is contributed by both BZ mechanism and BP mechanism, we can derive its total jet power for a thin accretion disk (Garofalo 2009; Garofalo et al. 2010):

$$P_{\rm jet}^{\rm Hybrid} = 2 \times 10^{47} \text{ erg s}^{-1} \alpha f^2 \frac{B_z}{10^5 \text{ G}} m_9^2 j^2, \tag{19}$$

where $m_9 = m/10^9$, α serves to establish the effectiveness of the BP jet as a function of spin, and f refers to the enhancement of the black hole by the disk through the magnetic field. Both the α and f parameters are interpreted under the Reynolds conjecture and are calculated using the Doppler factor (δ), or the black hole spin (j) as follows:

$$\alpha = \delta\left(\frac{3}{2} - j\right),\ f = -\frac{3}{2}j^3 + 12j^2 - 10j + 7 - \frac{0.002}{(j-0.65)^2} + \frac{0.1}{j+0.95} + \frac{0.002}{(j-0.055)^2}. \tag{20}$$

3. Results and Discussion

This study contains non-quasi-simultaneous observational data. For data to be considered quasi-simultaneous, it is required that different frequencies are observed in the same period. For instance, radiation in the high-energy band is produced and observed first, closely followed by the one in the low-energy band. However, the radiation regions for different bands are different. Specifically, the timescale for the γ-ray band is often minutes or hours, whereas the radio band could extend to weeks or months. Consequently, if observation of a previous flare in a low-energy band like the radio band is ongoing, the next flare might be simultaneously observed in the γ-ray band. The hypothesis is that at a specific observation interval, different bursts may be observed in different bands, indicating that even quasi-simultaneous observations can still be affected by delay effects. Therefore, the challenge of obtaining quasi-simultaneous data lies in resolving the time delay among different bands, an enduring problem for numerous FSRQs due to the lack of direct observational data.

3.1. Estimations for BLR Luminosity and Black Hole Mass

As discussed in Section 2.2, our BLR data is derived from significant samples from P21, Z22, and C24. The samples from P21 and Z22 are presented in the Fermi Large Area Telescope (LAT) Fourth Source Catalog Data Release 2 (4FGL-DR2; Abdollahi et al. 2020). The sample from C24, on the other hand, is collected in the 4FGL-DR4 catalog, the most updated version of survey data spanning the last 14 yr. This sample is further integrated with the 16th data release from the Sloan Digital Sky Survey (SDSS-DR16), along with the eighth data release of the Large Sky Area Multi-Object Fiber Spectroscopic Telescope (LAMOST-DR8).

During the spectral processing, the observed spectra were adjusted to the rest frame. The spectra obtained from the SDSS catalog or published articles have undergone correction for both airmass extinction and Galactic extinction, employing the extinction curve (Cardelli et al. 1989) and dust map (Schlegel et al. 1998). The methodology for data processing was comparatively rudimentary in the early sample collections. For example, some objects from P21 were digitized from plots or collected in tabular format, whereas some objects from Z22 did not take the PCA technique into consideration. This practice overlooked the variances between the central AGN and its host galaxy, and also disregarded potential Fe II emission lines originating from the optical band. Fortunately, the newly expanded data from C24 has incorporated a more detailed analysis. The strength of host galaxies at the red end of the spectrum, will affect the lines of Hα and Hβ. Then the light within the aperture of the telescope instrument includes light from both the central AGN and from the surrounding host galaxy. Utilizing the PCA method (Yip et al. 2004a, 2004b), we can determine the amount of light from the AGN and host galaxy, and separate these components accordingly. For light originating from the AGN, the Fe II emission line in the optical or UV band is a prominent feature of AGN and has an influence on continuum measurements. Consequently, optical and UV Fe II templates (Vestergaard & Wilkes 2001), together with a power law are adopted to fit the entire continuum. The continuum is then subtracted from the observed spectrum of the central AGN to derive the spectrum of emission lines. This spectrum is fitted with a Gaussian function to acquire the broad emission lines of Hα, Hβ, Mg II, and C IV. The component of the O III line is also included in the fitting procedure to eliminate the asymmetry caused by outflow. Due to the restriction placed by the resolution of the instrument, the triple absorption line of Ga near 4000 Å is indistinct, and the Balmer continuum at approximately 3000 Å in the rest frame is not accounted for.

The black hole mass, estimated via the RM technique, is generally reliable, though with its inherent limitations. On the one hand, the targeted source requires long-term multiple

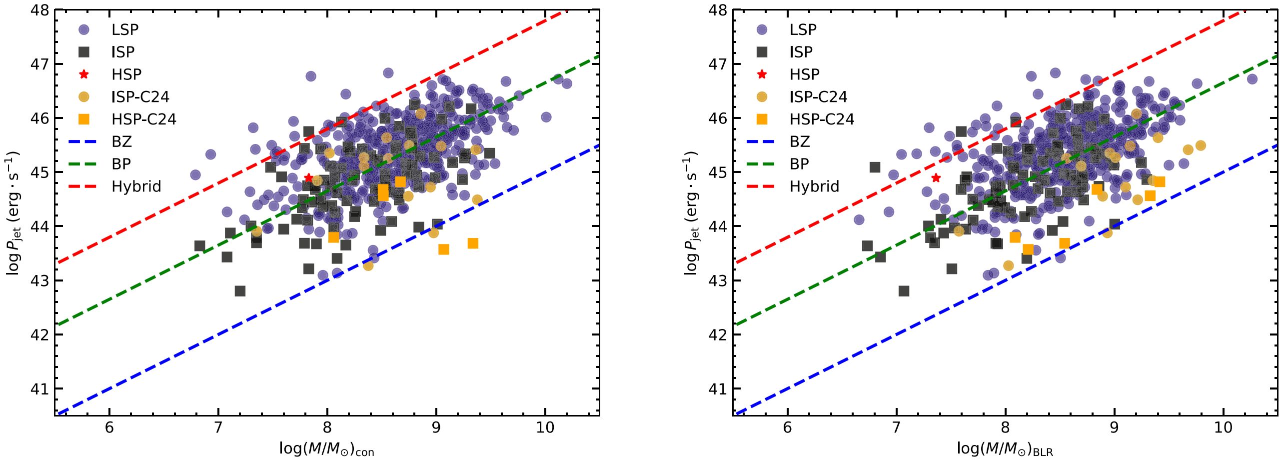

(a) (b)

Figure 4. In the left panel, the black hole mass ($\log(M/M_\odot)_{\rm con}$) is calculated by the traditional virial technique with continuum luminosity. In the right panel, the black hole mass ($\log(M/M_\odot)_{\rm BLR}$) is calculated solely by emission-line parameters. The maximal jet power as a function of the black hole mass. The blue-dashed line is the maximal jet power $P_{\rm jet}^{\rm BZ}$ extracted from a rapidly spinning black hole. The green-dashed line is the maximal jet power $P_{\rm jet}^{\rm BP}$ extracted from the accretion disk. The red-dashed line is the maximal jet power $P_{\rm jet}^{\rm Hybrid}$ in the hybrid model. Solid blue circles: LSP FSRQs; Solid black squares: ISP FSRQs; solid red star: HSP FSRQ; solid orange circles: LSP FSRQs from C24; solid orange squares: ISP FSRQs from C24.

monitoring, which is a challenging undertaking for a large number of sources. On the other hand, factors such as the BLR geometry, the BLR velocity structure, and the radiation position of the ionizing source demand consideration. Given the obscurity of these factors, they need to be determined based on various assumptions, potentially increasing the systemic errors of the estimated black hole mass (Krolik 2001). Nevertheless, some researchers have found the correlation of the BLR size with the luminosity at 5100 Å, enabling the estimation of black hole mass from the continuous spectral flux of the single observational spectrum and the FWHM of the emission line (Kaspi et al. 2000, 2005). However, due to the radiation contamination from components such as the relativistic jet (Scarpa & Urry 2002), accretion disk, host galaxy (Wu et al. 2004), or the DT, the black hole mass may be overestimated. Since the emission line is generated through photoionization by the radiation produced from the accretion disk and is free of the strong jet beaming effect, it serves as a viable replacement for the continuum luminosity in the calculation of black hole mass (Shen et al. 2011; Shaw et al. 2012). In our sample, if a source presents multiple broad lines, the black hole mass of each emission line is calculated and their geometric averages are then evaluated during the analytical process.

3.2. Jet Power versus Black Hole Mass

To obtain the jet power of BZ, BP, and hybrid models, we adopt several typical essential values: $\Omega_{\rm F} = 1/2$ signifying the maximum jet power (Ghosh & Abramowicz 1997), $\beta = 1$ denoting the maximal field strength advected by the corona, and $\xi_\phi = 1$ is required (Livio et al. 1999). Additionally, we consider $\tilde{\Omega} = 1$, $\tau_{\rm c} = 0.5$, and $\tilde{H}_{\rm c} = 0.5$ as common values for the corona parameters in the estimation (Cao 2009, 2018; Chen et al. 2022). The average Doppler factor obtained in Equation (8) as $\langle\delta\rangle = 8.58$ and a presumed black hole spin of $j = 0.95$, are adopted to calculate α and f. Then $R_{\rm ms}$ is calculated as follows:

$$\begin{cases} R_{\rm ms} = R_{\rm G}\{3 + Z_2 - [(3 - Z_1)(3 + Z_1 + 2Z_2)]^{1/2}\}, \\ Z_1 \equiv 1 + (1 - j^2)^{1/3}[(1 + j)^{1/3} + (1 - j)^{1/3}],\ Z_2 \equiv (3j^2 + Z_1^2)^{1/2}, \\ R_{\rm G} = \dfrac{GM_{\rm BH}}{c^2}. \end{cases} \tag{21}$$

Finally, the jet power of the BZ, BP, and hybrid mechanisms, each of them as a function of black hole mass, is presented in Figure 4. It reveals that the estimated black hole masses for approximately 97% of FSRQs fall within a range of 10^7–$10^{9.5}\ M_\odot$. The blue-dashed line denotes the BZ jet model, the green-dashed line represents the BP jet model and the red-dashed line stands for the hybrid jet model. Notably, the LSP FSRQs are denoted by blue circle dots, the ISP FSRQs by black square dots, and the HSP FSRQ by a distinct red star dot. In addition, a combination of orange circles and orange square dots represent the FSRQs newly expanded from C24. As evidenced in the diagram, the jet power of the hybrid model surpasses that of both the BZ and BP models.

In the left panel of Figure 4, the black hole mass is calculated by the traditional virial technique from the continuum luminosity. Interestingly, quite a few FSRQs, including an ISP FSRQ and several LSP FSRQs, are situated above the delineated hybrid dashed line. This observation posits a noticeable gap as no current model provides a satisfactory explanation for their jet power. Although the majority of FSRQs are found beyond the BZ dashed line and within the hybrid dashed line, the implication here is critical the BZ model may not sufficiently explain their jet power. On the contrary, four FSRQs from C24 that sit below the BZ dashed line suggest that the BZ model can sufficiently account for their jet power. Additionally, the distribution of the newly added FSRQs from C24 projects a significant dispersion and spans across three key regions: below the BZ dashed line, beyond the BZ dashed line and within the BP dashed line, and lastly, above the BP dashed line and below the hybrid dashed line.

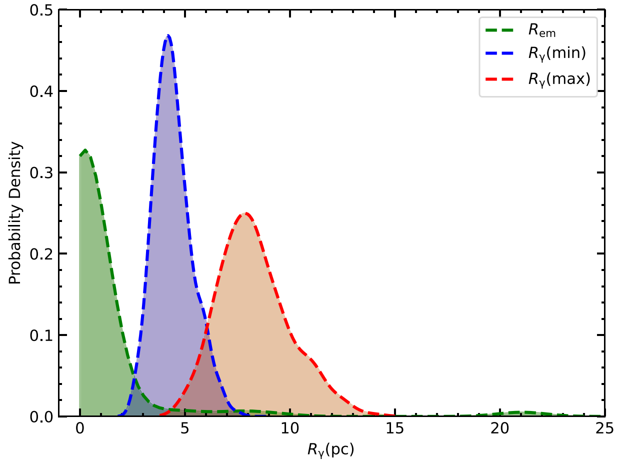

(a)

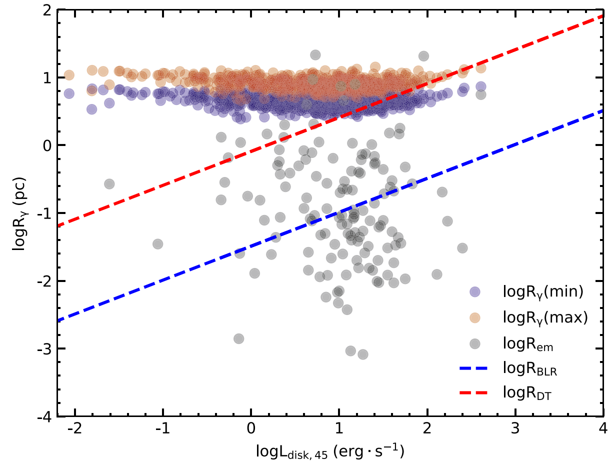

(b)

Figure 5. Left panel: distribution of the γ-ray dissipation region R_γ: the green-dashed histogram is for the $R_{\rm em}$ from Fan et al. (2023), the blue-dashed histogram is for the minimum R_γ, the red-dashed histogram is for the maximum R_γ. Right panel: Location of γ-ray dissipation region R_γ from the central black hole as a function of the disk luminosity: the blue circles are minimum $\log R_\gamma$, the red circles are maximum $\log R_\gamma$, and the black circles are the $\log R_{\rm em}$, the solid blue line and solid red line represent the BLR distance ($\log R_{\rm BLR}$) and the DT distance ($\log R_{\rm DT}$).

In the right panel of Figure 4, the black hole mass, calculated solely by emission-line parameters, is represented. The continuum luminosity, however, could be contaminated by the nonthermal component, which may overestimate the black hole masses derived from the continuum compared to the values obtained using only emission lines. Evidence of this phenomenon is reflected in the right panel of Figure 4, where more FSRQs are positioned above the upper left region of the hybrid dotted line, fewer FSRQs are situated below the lower right region of the BZ dotted line, and the number of FSRQs with black hole mass nearing 10 orders of magnitude of solar mass decreases from three to one, in comparison to the left panel. For the newly added FSRQs from C24, despite the presence of one outlier, an orange FSRQ above the BP dashed line, other orange FSRQs are primarily clustered in the region between the BZ and BP dashed lines. This pattern suggests that the BP model adequately interprets these FSRQs. Summarily, the BZ model is insufficient to account for the jet power in most FSRQs in our sample, the BP model only suffices for a limited number of FSRQs collected from C24, which possess a significantly lower jet power. The hybrid model, however, is likely the best explanation for the majority of our sampled FSRQs. The recent results of Chen et al. (2022) corroborate our findings, and they propose a hybrid model dominance in a sample of 16 γ-ray narrow-line Seyfert 1 galaxies.

3.3. Location of the γ-Ray-emitting Region

In the model proposed by Giovanoni & Kazanas (1990), the relativistic neutrons escape from the dense central region. These neutron particles subsequently decay into electrons and protons within a less dense region, and then produce π^0 and secondary electrons. The generation of γ-rays is then facilitated through IC scattering. Furthermore, the location of the γ-ray-emitting region (R_γ), can be constricted using either the variability timescale or the SED fitting. Liu et al. (2011) derived a formula to calculate R_γ using the method of variability timescale:

$$R_\gamma = \frac{R_{\rm BLR} + \frac{c\langle\tau_{\rm ob}\rangle}{1+z}}{\frac{c}{v_{\rm d}} - \cos\theta}. \tag{22}$$

In the above equation, $R_{\rm BLR}$ is the size of BLR, $\langle\tau_{\rm ob}\rangle$ symbolizes the observed time lag between broad lines and γ-rays caused by the light traveling time effects, $v_{\rm d}$ represents the traveling speed of disturbances down the jet, and θ is the angle between the jet axis and the line of sight. The size of the BLR ($R_{\rm BLR}$) and DT ($R_{\rm DT}$) can be given as the following formula derived from type 1 AGNs (Ghisellini & Tavecchio 2008):

$$\begin{cases} R_{\rm BLR} = 10^{17} L_{\rm d,45}^{1/2}\ {\rm cm}, \\ R_{\rm DT} = 2.5 \times 10^{18} L_{\rm d,45}^{1/2}\ {\rm cm}. \end{cases} \tag{23}$$

In addition, the observed time delay $\tau_{\rm ob}$ can adopt zero, negative, or positive values. When $\tau_{\rm ob} = 0$, γ-rays zero-lag broad lines, for $\tau_{\rm ob} < 0$, γ-rays will lead the lines, while for $\tau_{\rm ob} > 0$, γ-rays will lag the lines. The radiation emission from BLR or DT is characterized in the form of a blackbody spectrum (Ghisellini & Tavecchio 2009), and it is spiritedly debated whether the emission regions are located inside the BLR or outside the BLR. Considering the scenario where the radius (R_γ) is located within the BLR ($\tau_{\rm ob} < 0$), the photons of γ-ray above 10 GeV will be absorbed through photon–photon pair production (Liu & Bai 2006; Bai et al. 2009). Nonetheless, a mere 10% of blazars exhibit such spectral attenuation in γ-rays (Costamante et al. 2018). Consequently, the R_γ of γ-ray sources above 10 GeV were thought to be located outside the BLR remote from the black hole (Sikora et al. 2009; Tavecchio & Mazin 2009). This hypothesis is supported by other fitting results of broadband SEDs (Kang et al. 2014; Zheng & Yang 2016; Zheng et al. 2017; Tan et al. 2020), and blazar population studies (Arsioli & Chang 2018).

From this point, we consider the case where $\tau_{\rm ob} > 0$, indicating that the γ-rays lag broad lines. Our sample consists of a wide array of FSRQs, but the lack of complete spectral information prevents us from further analyzing the time delay between γ-rays and emission lines. For simplicity, we adopt the classical time delay as the average of our sample for the calculation. We take the time delay of 3C 273 as a canonical value with no zero-lag, and an average positive lag of $\langle\tau_{\rm ob}\rangle = 3.20$ yr, $v_{\rm d} = 0.9c - 0.995c$, and $\theta = 12°–21°$; see details from Liu et al. (2011) and reference therein. From Equation (22), we can obtain the minimum R_γ with $v_{\rm d} = 0.9c$ and $\theta = 21°$, and the maximum R_γ with $v_{\rm d} = 0.995c$ and $\theta = 12°$.

In this way, we get the R_γ(min) and R_γ(max) for the whole sample. The R_γ(min) values located within a range of 2.44–7.60 pc, with a mean value of 4.43 ± 0.90 pc, and the R_γ(max) values within a range of 4.57–14.25 pc with a mean value of 8.30 ± 1.69 pc. So far, neither the variability timescale nor the SED fitting can yield the distribution of R_γ for a larger sample of FSRQs. Therefore, we focus on the large amount of FSRQs recently studied by Fan et al. (2023), which obtained the distance from the central black hole to the emission region ($R_{\rm em}$) utilizing apparent velocity. The $R_{\rm em}$ of 147 FSRQs was reported, and we identified 134 common FSRQs from our sample ranging from 0.001–21.47 pc with a mean value of 0.88 ± 2.86 pc. Based on the above information, we compare R_γ(min) and R_γ(max) with $R_{\rm em}$. Their distributions are displayed in the left panel of Figure 5, from which we infer a sequence for the average values as $R_{\rm em} < R_\gamma(\rm min) < R_\gamma(\rm max)$.

In the right panel of Figure 5, the blue- and red-dashed lines denote the size of the BLR ($\log R_{\rm BLR}$) and the DT ($\log R_{\rm DT}$), respectively. The circle dots in red, blue, and black represent $\log R_\gamma$(max), $\log R_\gamma$(min), and $\log R_{\rm em}$. A significant dispersion exists between $\log R_{\rm em}$ and $\log L_{\rm disk,\,45}$, extending from within the BLR to beyond the DT, potentially indicating a rough correlation between the jet opening angle and viewing angle. This correlation might be illuminated by two instances: when the jet opening angle is marginally larger or smaller than the viewing angle, significant dispersion may be caused by the Doppler factor. In our calculations, both $\log R_\gamma$(max) and $\log R_\gamma$(min) are found to position above $\log R_{\rm BLR}$, demonstrating that the seed photons of FSRQs originate from the DT region in the EC process. Consequently, we present the upper and lower boundaries of average R_γ drawn from average positive lags that the γ-rays lag the emission lines ($\tau_{\rm ob} > 0$). This conclusion emphasizes the location of the dissipation region beyond the BLR or distant from the central black hole from other works (Fuhrmann et al. 2014; Zheng & Yang 2016; Zheng et al. 2017; Arsioli & Chang 2018; Jiang et al. 2020; Tan et al. 2020), aligns with our previous results.

4. Conclusion

This study compiles a comprehensive sample of FSRQs featuring broadband SEDs and broad emission lines. The jet power is obtained by constraining the physical parameters from the SED fitting parameters, while broad-line emissions are collected and extended to calculate the virial black hole mass utilizing two methods derived from the R–L relationship. The study also explores the dominant mechanism for the jet, focusing primarily on the jet power of the BZ model, BP model, and hybrid model. Furthermore, the correlation between synchrotron peak and IC peak luminosity is investigated to determine whether the IC component is primarily dominated by the SSC process or the EC process. Determination and comparison of the γ-ray emission region location with both the BLR size and the DT size were conducted to investigate the γ-ray emission region for FSRQs. The following conclusions are reached:

1. The hybrid model readily accounts for the jet power of FSRQs, given the correlation between jet power and black hole mass.
2. The relation between IC and synchrotron luminosities implies that the EC process is the primary contributor to the IC component in FSRQs.
3. The location of the γ-ray-emitting region is derived to be outside the BLR far away from the center black hole, under the average positive time lag between γ-rays and broad-line emissions.

Acknowledgments

We thank the anonymous referee for the useful comments and suggestions. L.X.Z. is grateful for the financial support from the National Natural Science Foundation of China (NSFC 12303018). This work is partially supported by the National Natural Science Foundation of China (NSFC U2031201, NSFC 11733001), and the Natural Science Foundation of Guangdong Province (2019B030302001). We also acknowledge the science research grants from the China Manned Space Project with No. CMS-CSST-2021-A06, Scientific and Technological Cooperation Projects (2020–2023) between the People's Republic of China and the Republic of Bulgaria. Thanks to Wu Xuebing and Zhou Ruixin for their help and suggestions.

ORCID iDs

Lixia Zhang https://orcid.org/0000-0003-3184-6896
Junhui Fan https://orcid.org/0000-0002-5929-0968

References

Abdo, A. A., Ackermann, M., Ajello, M., et al. 2010a, ApJ, 715, 429
Abdo, A. A., Ackermann, M., Ajello, M., et al. 2010b, ApJS, 188, 405
Abdo, A. A., Ackermann, M., Agudo, I., et al. 2010c, ApJ, 716, 30
Abdo, A. A., Ackermann, M., Ajello, M., et al. 2010d, ApJ, 712, 957
Abdollahi, S., Acero, F., Ackermann, M., et al. 2020, ApJS, 247, 33
Abdollahi, S., Acero, F., Baldini, L., et al. 2022, ApJS, 260, 53
Abramowicz, M. A., Chen, X. M., Granath, M., & Lasota, J. P. 1996, ApJ, 471, 762
Abramowicz, M. A., Lanza, A., & Percival, M. J. 1997, ApJ, 479, 179
Acero, F., Ackermann, M., Ajello, M., et al. 2015, ApJS, 218, 23
Ackermann, M., Ajello, M., Atwood, W. B., et al. 2015, ApJ, 810, 14
Agudo, I., Jorstad, S. G., Marscher, A. P., et al. 2011, ApJL, 726, L13
Ajello, M., Angioni, R., Axelsson, M., et al. 2020, ApJ, 892, 105
Angel, J. R. P., & Stockman, H. S. 1980, ARA&A, 18, 321
Arsioli, B., & Chang, Y. L. 2018, A&A, 616, A63
Arsioli, B., Fraga, B., Giommi, P., Padovani, P., & Marrese, P. M. 2015, A&A, 579, A34
Arsioli, B., & Polenta, G. 2018, A&A, 616, A20
Bahcall, J. N., Kozlovsky, B. Z., & Salpeter, E. E. 1972, ApJ, 171, 467
Bai, J. M., Liu, H. T., & Ma, L. 2009, ApJ, 699, 2002
Ballet, J., Bruel, P., Burnett, T. H., Lott, B. & The Fermi-LAT Collaboration 2023, arXiv:2307.12546
Barat, S., Chatterjee, R., & Mitra, K. 2022, MNRAS, 515, 1655
Blandford, R. D., & McKee, C. F. 1982, ApJ, 255, 419
Blandford, R. D., & Payne, D. G. 1982, MNRAS, 199, 883
Blandford, R. D., & Rees, M. J. 1978, Pittsburgh Conf. on BL Lac Objects, 328
Blandford, R. D., & Znajek, R. L. 1977, MNRAS, 179, 433
Błażejowski, M., Sikora, M., Moderski, R., & Madejski, G. M. 2000, ApJ, 545, 107
Bloom, S. D., & Marscher, A. P. 1996, ApJ, 461, 657
Böttcher, M., & Els, P. 2016, ApJ, 821, 102
Cao, X. 2009, MNRAS, 394, 207

Cao, X. 2018, MNRAS, 473, 4268
Cardelli, J. A., Clayton, G. C., & Mathis, J. S. 1989, ApJ, 345, 245
Celotti, A., Padovani, P., & Ghisellini, G. 1997, MNRAS, 286, 415
Chen, G., Zheng, Z., Zeng, X., et al. 2024, ApJS, 271, 20
Chen, L. 2014, ApJ, 788, 179
Chen, L. 2018, ApJS, 235, 39
Chen, Y., Gu, Q., Fan, J., et al. 2022, MNRAS, 517, 1381
Chen, Y., Gu, Q., Fan, J., et al. 2023, ApJS, 265, 60
Costamante, L., Cutini, S., Tosti, G., Antolini, E., & Tramacere, A. 2018, MNRAS, 477, 4749
Costamante, L., Ghisellini, G., Giommi, P., et al. 2001, in AIP Conf. Proc. 599, X-ray Astronomy: Stellar Endpoints, AGN, and the Diffuse X-ray Background, ed. N. E. White, G. Malaguti, & G. G. C. Palumbo (Melville, NY: AIP), 586
Dermer, C. D., Finke, J. D., Krug, H., & Böttcher, M. 2009, ApJ, 692, 32
Dermer, C. D., & Schlickeiser, R. 1993, ApJ, 416, 458
Dotson, A., Georganopoulos, M., Kazanas, D., & Perlman, E. S. 2012, ApJL, 758, L15
Fan, J., Xiao, H., Yang, W., et al. 2023, ApJS, 268, 23
Fan, J., Yang, J. H., Zhang, J. Y., et al. 2013a, PASJ, 65, 25
Fan, J. H., Yang, J. H., Liu, Y., & Zhang, J. Y. 2013b, RAA, 13, 259
Fan, J. H., Yang, J. H., Liu, Y., et al. 2016, ApJS, 226, 20
Fan, J. H., Kurtanidze, S. O., Liu, Y., et al. 2021, ApJS, 253, 10
Feigelson, E. D., & Babu, G. J. 1992, ApJ, 397, 55
Francis, P. J., Hewett, P. C., Foltz, C. B., et al. 1991, ApJ, 373, 465
Fuhrmann, L., Larsson, S., Chiang, J., et al. 2014, MNRAS, 441, 1899
Galeev, A. A., Rosner, R., & Vaiana, G. S. 1979, ApJ, 229, 318
Gao, X. Y., Wang, J. C., & Zhou, M. 2011, RAA, 11, 902
Garofalo, D. 2009, ApJ, 699, 400
Garofalo, D., Evans, D. A., & Sambruna, R. M. 2010, MNRAS, 406, 975
Gehrels, N. 1997, NCimB, 112B, 11
Ghisellini, G. 1996, in IAU Symp. 175, Extragalactic Radio Sources, ed. R. D. Ekers, C. Fanti, & L. Padrielli (Dordrecht: Kluwer), 413
Ghisellini, G., & Tavecchio, F. 2008, MNRAS, 387, 1669
Ghisellini, G., & Tavecchio, F. 2009, MNRAS, 397, 985
Ghosh, P., & Abramowicz, M. A. 1997, MNRAS, 292, 887
Giovanoni, P. M., & Kazanas, D. 1990, Natur, 345, 319
Gu, M., Cao, X., & Jiang, D. R. 2001, MNRAS, 327, 1111
Guo, H., Shen, Y., & Wang, S. 2018, PyQSOFit: Python Code to Fit the Spectrum of Quasars, Astrophysics Source Code Library, ascl:1809.008
Haardt, F., & Maraschi, L. 1993, ApJ, 413, 507
Hu, S. M., Chen, X., Guo, D. F., Jiang, Y. G., & Li, K. 2014, MNRAS, 443, 2940
Jiang, Y., Hu, S. M., Chen, X., Shao, X., & Huo, Q. H. 2020, MNRAS, 493, 3757
Jones, T. W., O'Dell, S. L., & Stein, W. A. 1974, ApJ, 188, 353
Kang, S. J., Chen, L., & Wu, Q. 2014, ApJS, 215, 5
Kaspi, S., Maoz, D., Netzer, H., et al. 2005, ApJ, 629, 61
Kaspi, S., Smith, P. S., Netzer, H., et al. 2000, ApJ, 533, 631
Komatsu, E., Smith, K. M., Dunkley, J., et al. 2011, ApJS, 192, 18
Krolik, J. H. 2001, ApJ, 551, 72
Laor, A. 2000, ApJL, 543, L111
Liu, H. T., & Bai, J. M. 2006, ApJ, 653, 1089
Liu, H. T., Bai, J. M., & Wang, J. M. 2011, MNRAS, 414, 155
Livio, M., Ogilvie, G. I., & Pringle, J. E. 1999, ApJ, 512, 100
MacDonald, D., & Thorne, K. S. 1982, MNRAS, 198, 345
Madejski, G. G., & Sikora, M. 2016, ARA&A, 54, 725
MAGIC Collaboration, Acciari, V. A., Ansoldi, S., et al. 2020, MNRAS, 496, 3912
Maraschi, L., Ghisellini, G., & Celotti, A. 1992, ApJL, 397, L5
Maraschi, L., & Tavecchio, F. 2003, ApJ, 593, 667
Marscher, A. P., & Gear, W. K. 1985, ApJ, 298, 114
Massaro, E., Perri, M., Giommi, P., & Nesci, R. 2004, A&A, 413, 489
Massaro, E., Tramacere, A., Perri, M., Giommi, P., & Tosti, G. 2006, A&A, 448, 861
McLure, R. J., & Dunlop, J. S. 2004, MNRAS, 352, 1390
Meier, D. L. 2001, ApJL, 548, L9
Nalewajko, K., Begelman, M. C., & Sikora, M. 2014, ApJ, 789, 161
Paliya, V. S., Böttcher, M., Gurwell, M., & Stalin, C. S. 2021, ApJS, 257, 37
Peterson, B. M. 1993, PASP, 105, 247
Poutanen, J., & Stern, B. 2010, ApJL, 717, L118
Ramakrishnan, V., Hovatta, T., Nieppola, E., et al. 2015, MNRAS, 452, 1280
Rees, M. J. 1967, MNRAS, 137, 429
Rybicki, G. B., & Lightman, A. P. 1979, AstQ, 3, 199
Scarpa, R., & Falomo, R. 1997, A&A, 325, 109
Scarpa, R., & Urry, C. M. 2002, NewAR, 46, 405
Schlegel, D. J., Finkbeiner, D. P., & Davis, M. 1998, ApJ, 500, 525
Shakura, N. I., & Sunyaev, R. A. 1973, A&A, 24, 337
Shaw, M. S., Romani, R. W., Cotter, G., et al. 2012, ApJ, 748, 49
Shen, Y., Richards, G. T., Strauss, M. A., et al. 2011, ApJS, 194, 45
Sikora, M., Begelman, M. C., & Rees, M. J. 1994, ApJ, 421, 153
Sikora, M., Stawarz, L., Moderski, R., Nalewajko, K., & Madejski, G. M. 2009, ApJ, 704, 38
Svensson, R., & Zdziarski, A. A. 1994, ApJ, 436, 599
Tan, C., Xue, R., Du, L. M., et al. 2020, ApJS, 248, 27
Tavecchio, F., & Mazin, D. 2009, MNRAS, 392, L40
Tramacere, A., Cavazzuti, E., Giommi, P., Mazziotta, N., & Monte, C. 2010, in AIP Conf. Proc. 1223, Science with the New Generation of High Energy Gamma-ray Experiments, ed. C. Cecchi et al. (Melville, NY: AIP), 79
Urry, C. M., & Padovani, P. 1995, PASP, 107, 803
Vestergaard, M., & Peterson, B. M. 2006, ApJ, 641, 689
Vestergaard, M., & Wilkes, B. J. 2001, ApJS, 134, 1
Wandel, A., Peterson, B. M., & Malkan, M. A. 1999, ApJ, 526, 579
Wu, X. B., Wang, R., Kong, M. Z., Liu, F. K., & Han, J. L. 2004, A&A, 424, 793
Yang, J., Fan, J., Liu, Y., et al. 2023, SCPMA, 66, 249511
Yang, J. H., Fan, J. H., Liu, Y., et al. 2022, ApJS, 262, 18
Yip, C. W., Connolly, A. J., Szalay, A. S., et al. 2004a, AJ, 128, 585
Yip, C. W., Connolly, A. J., Vanden Berk, D. E., et al. 2004b, AJ, 128, 2603
Zhang, J., Liang, E. W., Zhang, S. N., & Bai, J. M. 2012, ApJ, 752, 157
Zhang, L., Chen, S., Xiao, H., Cai, J., & Fan, J. 2020, ApJ, 897, 10
Zhang, L., Liu, Y., & Fan, J. 2022, ApJ, 935, 4
Zhang, L., Yang, J., Liu, Y., & Fan, J. 2023, SCPMA, 66, 109511
Zheng, Y. G., Kang, S. J., Yang, C. Y., & Bai, J. M. 2020, MNRAS, 499, 1188
Zheng, Y. G., & Yang, C. Y. 2016, MNRAS, 457, 3535
Zheng, Y. G., Yang, C. Y., Zhang, L., & Wang, J. C. 2017, ApJS, 228, 1